# Features of "fishtail" shock interaction in transonic flows on a NACA0012 profile

Renato Paciorri *
*University of Rome "La Sapienza", Rome, Italy, 00184*

Aldo Bonfiglioli†
*University of Basilicata, Potenza, Italy, 85100*

Alessia Assonitis‡
*University of Rome "La Sapienza", Rome, Italy, 00184*

**Slender profiles flying at nearly sonic speed exhibit a peculiar shock-pattern, which is commonly referred in literature as the "fishtail" shock-structure. It consists of two oblique shock waves that originate at the trailing edge of the airfoil and interact with a detached, nearly normal shock wave in two triple-points located along the oblique shocks. Making use of both shock-fitting and shock-capturing CFD simulations and classical shock-polar analysis, we prove that, in the case of a NACA0012 airfoil, the two interaction points cannot be modeled using the three shocks theory that von Neumann developed nearly a century ago to describe triple-points arising in Mach reflections. Our analysis suggests that the four-waves interaction model proposed by Guderley should be used instead.**

## Nomenclature

$c$ = airfoil's chord in meters

$m$ = number of physically admissible solutions

$M_i$ = Mach number in region $i$

$p$ = pressure made dimensionless using twice the free-stream dynamic pressure

$X_s$ = distance (in meters) between the trailing edge and the nearly normal shock

$\alpha$ = angle of attack in degrees

$\gamma$ = adiabatic index

$\delta$ = $(\gamma - 1)/2$

$\theta_{ij}$ = flow deflection (in degrees) across the discontinuity separating regions $j$ and $i$

$\sigma_{ij}$ = slope of the shock separating the shock-upstream region $i$ from the shock-downstream region $j$

*Associate professor, Dept. of Mechanical and Aerospace Engineering, Via Eudossiana 18 - Roma , Italia 00184.
†Associate professor, School of Engineering, Via dell'Ateneo Lucano 10 - Potenza, Italia, 85100.
‡Research fellow, Dept. of Mechanical and Aerospace Engineering, Via Eudossiana 18 - Roma , Italia 00184.

$\mu^2$ = $(\gamma - 1)/(\gamma + 1)$

$\nu$ = Prandtl-Mayer function

$\xi_{ji}$ = Pressure ratio: $p_j/p_i$

$\xi_i$ = Inverse pressure ratio: $p_1/p_2$

$\infty$ = free-stream condition

## I. Introduction

Depending on the flight Mach number, the transonic flow past the profile of an airfoil can feature a peculiar shock-interaction pattern called "fishtail". Figure 1, which is taken from a 1950s documentary, titled " High

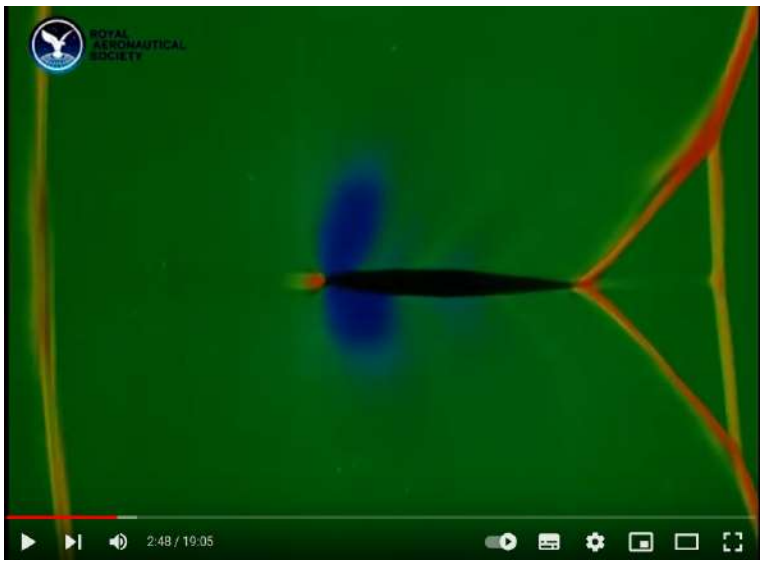


**Fig. 1 Transonic fishtail: experimental visualization re-printed from Shell Film Unit, 'High Speed Flight : Part 2-Transonic Flight', 1959. [1].**

Speed Flight : Part 2 -Transonic Flight ", produced by the Shell Film Unit [1] shows that the airfoil plays the role of the body of the fish, whereas the fishtail consists in two oblique shock waves that originate at the trailing edge (TE) and a nearly normal shock wave standing at some distance behind. The nearly normal shock joins the two oblique shocks in two interaction (or branching) points. Each of these shall be referred to as a "triple-point" (TP), because of the confluence of three different shock waves, as shown in the sketch of Fig. 2.

The formation of a TP is more often associated with the reflection of a shock wave from a solid surface, a phenomenon that can be viewed under two different perspectives: either i) as a steady phenomenon, whereby an oblique shock wave impinges on a wall or as ii) an unsteady phenomenon, whereby a moving normal shock wave encounters a wedge. Although these two phenomena may seem very different, they are in fact quite similar, because we can turn the unsteady problem into a pseudo-stationary one by using a change of variables, see e.g. [2]. Over 140 years ago, Ernst Mach (see

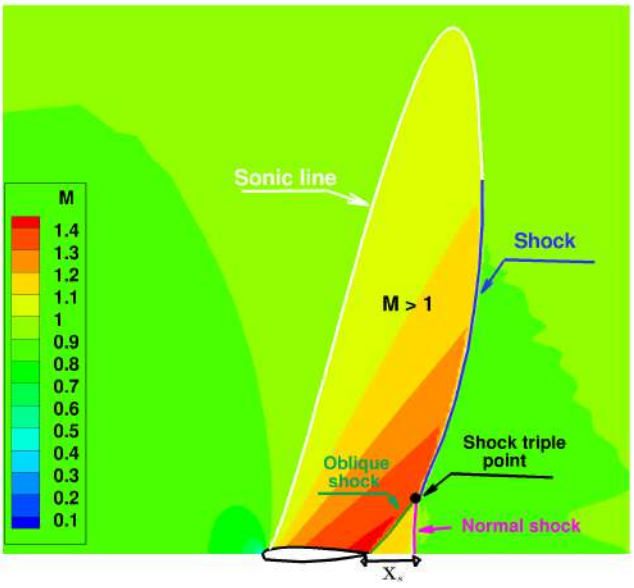


**Fig. 2 Transonic fishtail: computed Mach flow-field around the NACA0012 airfoil**

the review [3] on his and related experiments) showed that two distinct patterns arise in the unsteady reflection of a shock wave from a wedge: the regular and the irregular one. In regular reflection, the oblique incident shock reflects as an oblique shock wave of the opposite family and the incident and reflected shocks share an interaction point on the wall. The irregular reflection features a triple-point located close to (but not on) the wall where three different shock waves meet: the incident shock (I-shock), the reflected shock (R-shock), and a strong shock called Mach stem (M-shock), which reaches the solid surface. Moreover, since it can be proved that "Three shocks separating three zones of different continuous states are impossible" [4, § 129], there is also a contact discontinuity emanating from the TP. In the 1940s, von Neumann [5–7] proposed an analytical model, known as the three-shock theory (3ST), to compute the flow at the TP. However, von Neumann's model cannot explain some cases of weak* Reflections where the presence of the TP is observed experimentally and numerically, but the 3ST does not predict. This inconsistency has given rise in the literature to the "von Neumann paradox", which has been the subject of several theoretical, experimental and numerical studies. One possibility to reconcile theory and experiments consists in postulating a different wave structure at the TP. According to the review by Pain and Rogers [9], Bargmann and Montgomery [10] were the first ones to propose the addition of an isentropic expansion at the TP to obtain a solution to those cases not covered by the 3ST. Two years later, the four-waves theory (4WT, the fourth wave being the centered expansion fan) was further elaborated by Guderley [11], see also his book on transonic flow [12, pag. 147]. In Guderley's work, it is suggested that a complex supersonic patch develops behind the R-shock, originating from the expansion fan centered at the TP. The homentropic model proposed

*in the present context by the term "weak" we refer to the strength of the I-shock, see [8, § 11.11] for a more precise taxonomy.

by Guderley did not include the contact discontinuity which was added, fifteen years later, by Kalghatgi and Hunt [13]. This is the earliest occurrence that we have been able to find in the literature where the modified Guderley's model (i.e. the non-homentropic 4WT including the contact discontinuity) is described.

In this paper we show that the local flow conditions that prevail close to the TP of a fishtail shock-pattern fall outside the domain of applicability of von Neumann's 3ST, and should be modeled instead using Guderley's 4WT.

The paper is organized as follows. Section II provides background information on the problem at hand, including details of the three-shock and four-wave theories and their respective domains of existence. Shock-capturing and hybrid shock-capturing/shock-fitting simulations are reported in Sect. III and the results of the latter are combined with classical shock-polar analysis in Sect. IV to draw the main conclusions of this study. These are further corroborated in Sect. V where the results of a shock-fitting simulation which incorporates Guderley's model are reported. Conclusions are drawn in Sect. VI and Appendix VI gives the equations defining the boundaries of the domains of existence of the 3ST and 4WT.

## II. Background

### A. Transonic fishtail

Although the fishtail shock-pattern is frequently encountered in transonic flows, it is difficult to find either experimental or numerical studies addressing this topic in the literature.

As far as computational studies are concerned, the transonic flow past a NACA0012 airfoil at free-stream conditions $M_\infty = 0.95$ and zero angle of attack ($\alpha = 0°$), which features a fishtail shock-pattern, was one among several test-cases proposed during the ICASE-LaRC Workshop on Adaptive Grid Methods in 1995 [14]. Figure 2, re-printed from the Workshop proceedings, displays a sketch of the flowfield of this test-case, which is named AGARD03.

Among the workshop contributors who engaged in the AGARD03 test-case, Richter and Leyland [15] examined the effect of the far-field location on the aerodynamic forces and the position, $X_s$, of the nearly normal shock. They found that, even using feature-adapted meshes, the shock-induced drag was converged to four significant digits by placing the far-field 300 chords away from the airfoil, but $X_s$ keeps changing by almost 2% when the far-field is moved further away to 10,000 chords.

Since then, due to its fairly complex shock-interaction pattern, the AGARD03 test-case has been subject of a number of computational studies, see e.g. [16], especially those dealing with mesh adaptation. We have not found, however, any computational or theoretical study addressing the flow structure at the TP.

### B. The three-shock theory

The flow pattern in the neighborhood of the TP of Fig. 1 is schematically shown in Fig. 3, borrowing the nomenclature used for Mach reflections: the oblique shock emerging from the TE of the airfoil is the I-shock, which can be thought of

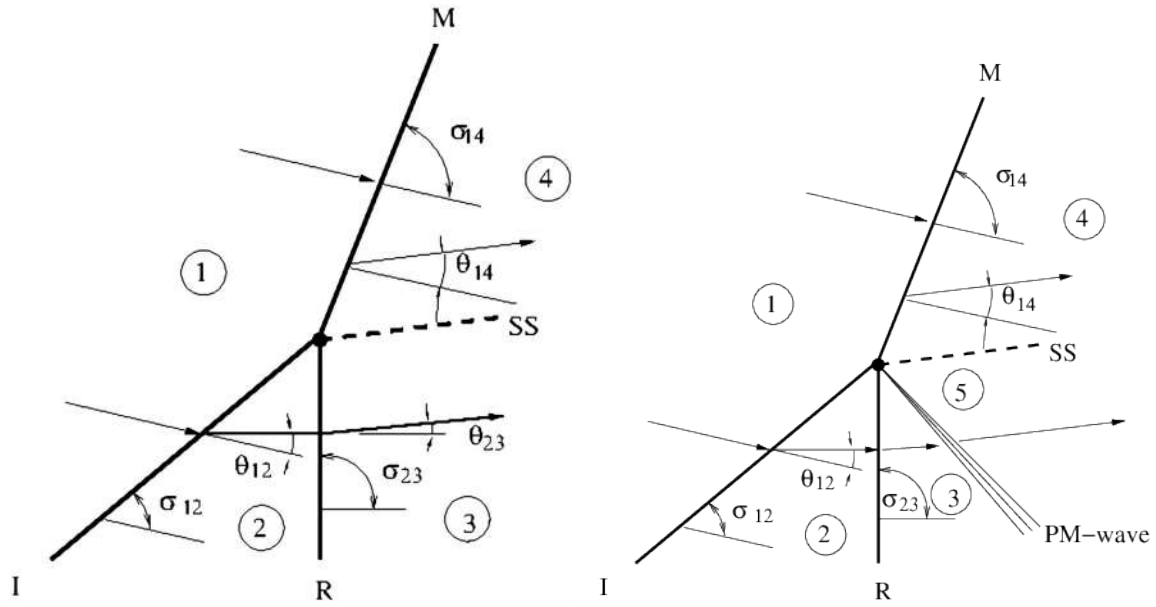


(a) 3ST (b) 4WT

**Fig. 3 Flow in the neighborhood of a TP according to von Neumann's (3ST) and Guderley's (4WT) models; all angles are relative to the flow upstream of the previous shock**

as being "reflected" by the far field, thus giving rise to the nearly normal shocks (the R-shock). Beyond the branching point where the oblique and nearly normal shock interact, the former bends into the M-shock; the dashed line represents the contact-discontinuity or slip-stream (SS).

The non-linear algebraic equations governing the 3ST, which can be found in either [4, § 135] or [17, § 1.3.2], consist in the Rankine-Hugoniot jump relations for all three shocks, supplemented by the condition of parallel streams and equal pressure across the contact discontinuity. The number of unknowns matches that of the available equations once three parameters are given. We assign: *i*) the adiabatic index, $\gamma$, of the gas (which we assume to behave like a perfect gas); *ii*) the Mach number, $M_1$, ahead of the I-shock and *iii*) a measure of the I-shock strength, which we here choose to be the I-shock angle, $\sigma_{12}$. A powerful graphical tool for determining solutions to the 3ST consists of seeking intersections between the I- and R-shock polars in the pressure-deflection $(\theta, p)$ plane. For given values of $\gamma$ (here always set equal to 1.4) and $M_1$ (four separate values chosen here in a narrow range), there is an unique shock polar in the $(\theta, p)$ plane. Four such polars are shown as dotted curves in the the four subfigures of Fig. 4. We determine the point on this polar that corresponds to a given deflection $\theta_{12}$, and we draw another shock polar centered on this point (that we will call the "knot"). If the two polars intersect (as they do at the points represented by symbols in Fig. 4), then that point marks a state that could be reached either by a single shock (the M-shock), or by two shocks (the I-shock and then the R-shock). By doing so, we have found a possible solution to the flow in Fig. 3a. Henderson [18] has shown that seeking the intersection(s) between the I- and R-shock polars amounts to compute the real roots of a tenth-degree polynomial in the unknown pressure ratio $\xi_{41} = p_4/p_1 = p_3/p_1$ across the M-shock, i.e. the ordinates of the points

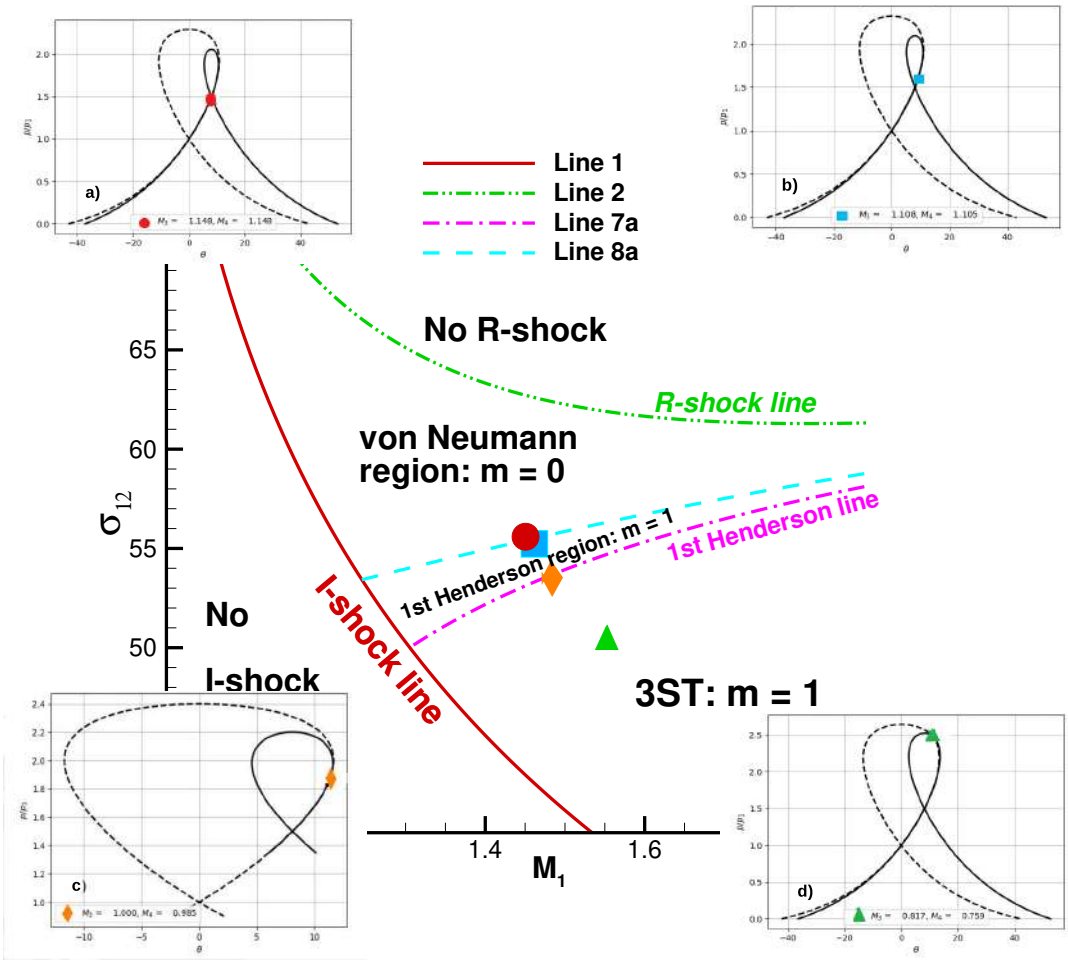


**Fig. 4 Domain of existence of solutions to the 3ST and transition boundaries between various shock-wave configurations in the $(M_1, \sigma_{12})$ plane; also shown are pressure-deflection diagrams corresponding to four different pairs of $(M_1, \sigma_{12})$ values.**

marked by symbols in the $(p, \theta)$ plane of the four insets of Fig. 4. Since two real roots are known and have multiplicity two, the polynomial order can be reduced to six. Moreover, not all real roots correspond to flow patterns that can be accepted on physical grounds and the number $m$ of physically admissible solutions depends upon the aforementioned three parameters: $\gamma$, $M_1$ and $\sigma_{12}$. If a diatomic gas is chosen, i.e. $\gamma = 7/5$ as we do here, Henderson [18] has shown that $m = 0, 1, 2, 3$, depending on the values taken by the remaining two parameters: $M_1$ and $\sigma_{12}$. Therefore, a convenient way to look at the existence and features of the solutions to the 3ST consists in using the $(M_1, \sigma_{12})$-plane. Our four choices for the pair $(M_1, \sigma_{12})$ are marked using different symbols in the main figure. These points have been selected since they give rise to four different outcomes, each shown in the corresponding subfigure, that is typical of the situation in its region of the $(M_1, \sigma_{12})$ plane.

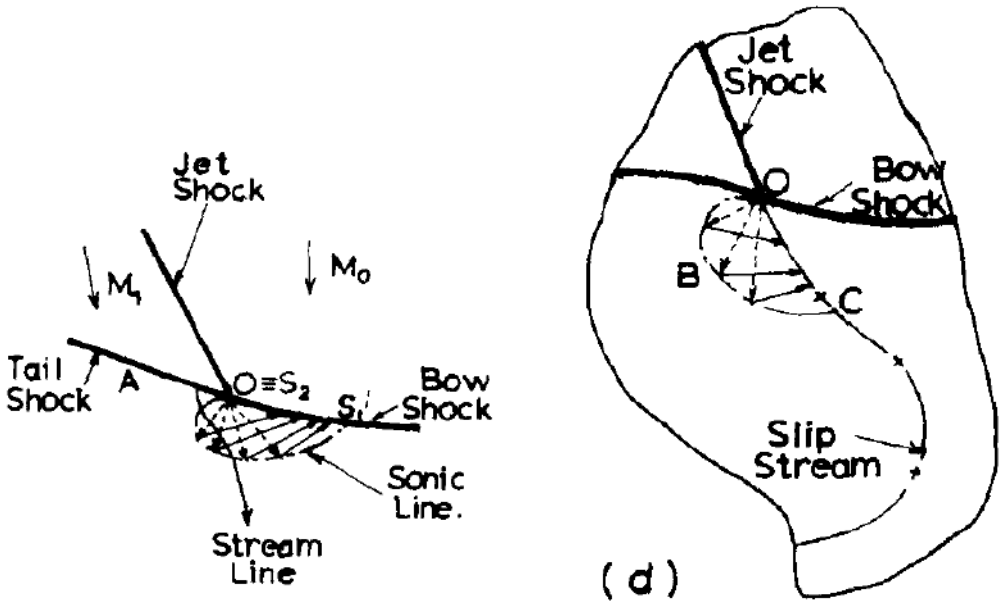


(a) Homentropic model (b) Non-homentropic model

**Fig. 5 Sketches of the original and modified (by the addition of the SS) Guderley's model. Source: Kalghatgi et al. [13]; reprinted with permission of the Aeronautical Journal (Royal Aeronautical Society) (1975).**

### C. The four-waves theory

A sketch of Guderley's four-wave model, both in the homentropic and non-homentropic case, is shown in Fig. 5, which has been reprinted from [13]. Both frames of Fig. 5 show a supersonic pocket surrounded by subsonic flow; inside the supersonic region, an expansion fan originates at the TP and is reflected from the sonic line, giving rise to compression waves that reach the M-shock in the homentropic case and the SS in the non-homentropic one. Indeed, the key difference between the two cases lies in the presence of the SS, which is absent in the former. For the homentropic model, Khalghatgi and Hunt [13, pag. 120] and Hunter & Brio [19, pag. 250] have shown that the sonic line must pass exactly through the TP; by reference to Fig. 5a, this amounts to saying that the sonic point $S_2$ must coincide with point $O$, which denotes the TP in Fig. 5. In the non-homentropic case, Khalghatgi and Hunt [13, pag. 120] "conclude, with some confidence, that the tail shock[†] flow will be sonic at the triple point" because departure from homentropic flow conditions is expected to be small inside the supersonic bubble.

Therefore, if we agree with this stance, as also Vasi'lev et al. [20] do, the 4WT proposed by Guderley and modified by Khalghatgi and Hunt [13] by including the SS, consists in an R-shock that decelerates the flow to sonic condition at the TP, followed by an expansion fan, centered at the TP, which accelerates the flow from sonic to supersonic speed, see the sketch in Fig. 3b. The flow downstream of the R-shock is sonic at the TP, but subsonic as one moves away from the

[†]the jet, tail and Mach shocks of Fig. 5 corresponds to the I-, R- and M-shock of Fig. 3b.

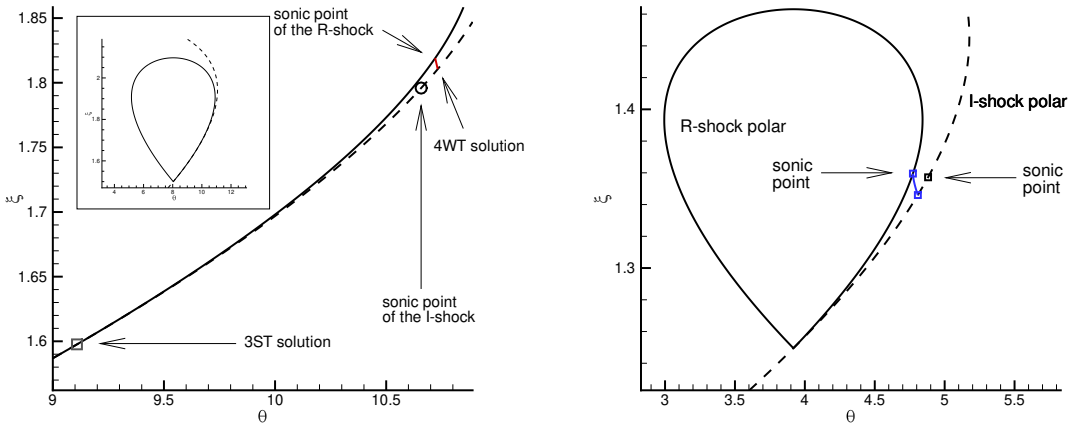


(a) Vasil'ev reflection: $M_4 < 1$.

(b) Guderley reflection: $M_4 > 1$.

**Fig. 6 Vasil'ev and Guderley reflection: shock polars in the $(p, \theta)$ plane**

.

TP, along the R-shock. Inside the subsonic region bounded by the R-shock and the sonic line of the bubble, Vasilev et al. [21] observe that: "it is the wave curvature which results in the acceleration of the flow from subsonic to sonic conditions" along the head of the EF. Indeed, pressure and density gradients along the R-shock are clearly visible in recent numerical simulations, see [22, Fig. 9(c)] and [20, Fig. 3(a)], thus indicating that the R-shock is curved. On the other side of the SS Kalghatgi and Hunt [13] noticed that the flow can be either subsonic or supersonic; in the former case the flow pattern is referred to as a Vasil'ev reflection (VR), whereas in the latter as a Guderley reflection (GR) [17]. In the $(p, \theta)$ plane the 4WT amounts to connect the sonic point of the R-shock polar with the I-shock polar using a Prandtl-Mayer expansion; this is shown in Figs. 6a and 6b for the VR and GR, respectively. The non-linear algebraic equations governing the 4WT are reported in Appendix VI, where the two sets of data used to draw the sample VR and GR of Fig. 6 are also listed.

### D. Domain of existance of the 3ST and 4WT

A convenient way to look at the domain of existence and features of the solutions to the 3ST and 4WT consists in using the $(M_1, \sigma_{12})$-plane shown in the main frame of Fig. 4 where we restricted the abscissae to the $M_1$-range that is relevant to the current application and we have drawn only a subset of the various curves that mark the boundaries between regions featuring different shock-interaction patterns.

The features of the solution along the four lines drawn in Fig. 4, and inside the regions they bound, will now be briefly summarized, whereas the equations needed to draw the lines are given in Appendix VI. The labeling of the various lines and regions follows [8, § 11].

On line 1 the I-shock is a Mach wave and, therefore, there can be no I-shock for points below line 1. On line 8a, the intersection between the two polars takes place at the knot of the R-shock polar, see Fig. 4a. As $M_1$ increases, line 8a asymptotically approaches line 2, which is where the flow behind the I-shock is sonic. Therefore, shock-reflection is impossible above line 2. On line 7a, which is called the first Henderson line, the flow behind the R-shock is exactly sonic; see Fig. 4c. Inside the so-called von Neumann region, which is the region above line 1, below line 2 and bounded to the right by line 8a, Henderson [18] has shown, see also [8, § 11.11], that there are no solutions to the 3ST, i.e. $m = 0$. However, the confluence of three shock-waves at a TP has been observed experimentally, see e.g. [23], also for values of $(M_1, \sigma_{12})$ that fall inside the von Neumann region. This contradiction between experimental evidence and 3ST is referred in literature as the von Neumann paradox [24]. Lines 1, 8a and 7a bound the first Henderson region, where $m = 1$ and the flow behind the R-shock is supersonic, see Fig. 4b; to the right of line 7a: $m = 1$ and the flow behind the R-shock is subsonic, see Fig. 4d. We will not discuss the case when there is more than one solution to the 3ST, i.e. $m > 1$, because it occurs when $M_1$ takes values larger than those of interest here.

According to [17] and [21], the transition between the 3ST and 4WT takes place along the first Henderson line, or line 7a in Fig. 4, where the Mach number behind the R-shock in the 3ST is sonic. This is because line 7a also coincides with the line where the 4WT features a vanishing expansion fan. Indeed, when the EF has zero strength, see the sketch of Fig. 3b, region 5 disappears by merging with region 3 and the 4WT reduces to the 3ST with unit Mach number behind the R-shock.

Inside the first Henderson region, where the flow behind the R-shock is supersonic, both 3ST and 4WT solutions are possible; an example is shown in Fig. 6a, which refers to the point marked with a square in Fig. 4. According to the same authors [17, 21], however, the 3ST solutions inside the first Henderson region should be discarded as un-physical, because of the supersonic Mach number behind the R-shock, and should be replaced by the 4WT. Therefore, the 3ST applies to the right of the first Henderson line and the 4WT to its left. Moreover, solutions to the 4WT also exist to the left of line 8a, i.e. inside the von Neumann region, which implies that the 4WT offers a solution to the von Neumann paradox.

Wind-tunnel visualizations obtained by [25], see also [26, 27], using an ad-hoc designed experimental facility seem to confirm the complex flow structure of Guderley's model, in particular the existence of the expansion fan. The earliest calculations showing a Guderley-type reflection pattern are those performed by Vasil'ev [28, 29] solving the Euler equations. Similar results were obtained for the Euler equations in [22, 30] and calculations showing an interaction pattern compatible with Guderley's model have also been obtained when numerically solving the unsteady transonic small disturbance equations, see [31], the nonlinear wave system (a simplified version of the isentropic Euler equations), see [32], and the shallow waters equations, see [33, 34]. Two remarkable features of Guderley's solution are the smallness of the supersonic patch, which possibly explains why it has for long gone unnoticed both in experiments and simulations, and the apparent existence of not a single, but rather an array of supersonic patches of decreasing

size, see [22, 33]. These features make the numerical simulation of the GR/VR very challenging. In recent work, Vasil'ev [20] used a structured-grid, front-tracking code to simulate the irregular oblique-shock reflection from a flat wall in the parameter range where GR and VR occur. Adequate resolution was obtained by progressively reducing the size of the computational domain surrounding the TP.

To conclude this section, we mention that the numerical simulations performed by Ivanov and co-workers [35], making use of both DSMC and Euler/Navier-Stokes models, once combined with standard shock polar analysis, reveal that Guderley's 4WT is indeed recovered in the limit of very high Reynolds number.

## III. Numerical simulations of transonic flows past a NACA0012 profile

In order to gain insight into the flow structure at the TP of the fishtail shock-pattern, we have run three different sets of simulations of the AGARD03 test-case which differ in the way the various discontinuities, and their mutual interaction, are modeled. All three simulations have been performed using the in-house, open-source CFD code *UnDiFi-2D*, which can be freely downloaded from a public repository, see [36]. The code is capable of computing 2D inviscid steady or unsteady flows on unstructured triangular grids using three different shock-modeling options: fully-fitted, hybrid and fully-captured. When run in fully-fitted mode, all shocks and slip-streams are "fitted", i.e. treated as discontinuities of zero thickness, see[37, 38] for algorithmic details. In addition, also those branching points where different discontinuities meet are treated as geometrical points (0-dimensional) and modeled as described in [39, 40]. In the present context, this is the case of the TP arising in the fishtail shock-pattern. When run in "hybrid" mode, only some of the discontinuities are fitted while all others are captured, including the interaction between a fitted and a captured discontinuity. When run in "fully-captured" mode, all discontinuities are captured using the shock-capturing `eulfs` code [41, 42] which is also used in all three simulation modes to discretize the governing PDEs in the smooth regions of the flow-field. `eulfs` is an unstructured, vertex-centered CFD code which relies on Residual Distribution (also known as Fluctuation Splitting) schemes for spatial discretization. Algorithmic details can be found in [41, 42], where it is shown that the code delivers second-order-accuracy, both in space and time, in smooth flows. In the presence of shock waves, it is shown in [43] that the fully-fitted approach allows to retain the design (second) order-of-accuracy of the scheme within the entire shock-downstream region, whereas the fully-captured approach reduces to first order-of-accuracy behind the shocks. This is a flaw of the shock-capturing approach which has been known for long [44, 45], but is often understated.

Fig. 7 shows the computational domain and three different zooms of the triangular mesh being used. The outer boundary is a circle of radius R/c = 100 centred at the leading edge of the profile: the choice of R was based on the computations performed by Richter and Leyland [15], and aims to find a compromise between keeping a reasonable computational cost and getting an almost mesh-independent location of the nearly normal shock. As shown in the three frames of Fig. 7, we have used three levels of decreasing mesh spacing over the computational domain. The finest mesh spacing (h/c = 0.030), see Figs. 7b and 7a, has been used inside the pentagonal region that surrounds the airfoil and

covers the entire shock pattern, including the supersonic pockets on both sides of the airfoil. A coarser mesh spacing (h/c = 0.6285) has been used within the elliptical region of Fig. 7a, which serves the only purpose of smoothly bridging the regions where the finest and coarsest mesh spacing have been used. The pentagonal and elliptical regions have been meshed using the Triangle code [46], whereas the frontal/Delaunay mesh generator described in [47] has been used to bridge the boundary of the elliptical region with the outer boundary, see Fig. 7c. The overall mesh, which is made of 139570 grid-points and 278753 triangles, has been built without taking into account flow symmetry about the airfoil's chord. This grid shall be referred to in the following as the baseline or un-adapted or level 0 grid. The grids used to perform the hybrid and fully-fitted simulations are nearly identical to the baseline grid, except for minor differences in the neighborhood of the fitted discontinuities.

In the hybrid calculation the two oblique shocks originating at the TE, both above and below the profile, are fitted, whereas the nearly normal shock is captured. Each of the two oblique shocks is fitted starting at the TE up to the point where is weakens into a Mach wave, well beyond the TP where the oblique shocks interact with the nearly normal shock. By reference to the sketch in Fig. 3, the I- and M-shocks are fitted, whereas the R-shock is captured. As mentioned earlier, in the hybrid simulation, the interaction between the nearly normal shock and the two fitted oblique shocks is captured, not modeled. As a result, the TP is not a geometrical point, but a region whose size is comparable to the numerical thickness of the nearly normal shock. Figure 8shows the pressure field computed in the hybrid simulation: to improve readability, we mark the two fitted oblique shocks by using a solid (red) line, even if their numerical thickness is zero. In contrast, the build-up of isobar contour lines allows to identify the nearly normal shock downstream of the TE in Fig. 9b. It shows that the numerical thickness of the captured shock is finite and it spans two to three cells.

In order to validate the `UnDiFi-2D` solution displayed in Fig. 8, we have performed a code-to-code comparison using two different vertex-centred, open-source CFD solvers: `NEO` and `SU2`. `NEO`, which is part of the `UnDiFi-2D` software package, relies on the same type of Residual Distribution schemes [48, 49] also used in the `eulfs` code. In contrast, `SU2` [50], which is one of the public domain CFD codes more widely used nowadays, relies on a second-order-accurate Finite Volume discretization.

Figure 9, where Mach iso-contour lines are drawn, allows to compare the hybrid shock-fitting simulation with the fully-captured simulations obtained using `NEO` and `SU2`. All three simulations have been run on the baseline mesh shown in Fig. 7. Figure 9 reveals excellent mutual agreement among the three sets of calculations: observe, in particular, that the fitted shocks (marked using solid blue lines) fall within the finite thickness of the captured shocks computed using both `SU2` (solid red line) and `NEO` (dotted green line).

Moreover, in order to show that the resolution of the baseline mesh is adequate, we have also performed a mesh refinement study by coupling the `SU2` code with the `MMG` [51, 52] adaptive mesh generator. Using the density gradient computed by `SU2` on the baseline mesh, two mesh-adaptation cycles have been performed as summarized in Tab. 1, where level 0 refers to the un-adapted (or baseline) mesh in Fig. 7. Figure 9 compares the hybrid shock-fitting solution

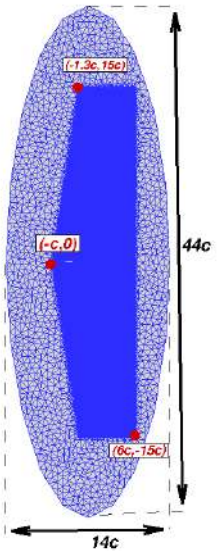


(a) Mesh inside the elliptical region.

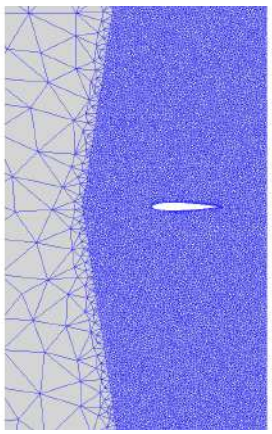

(b) Mesh around the airfoil.

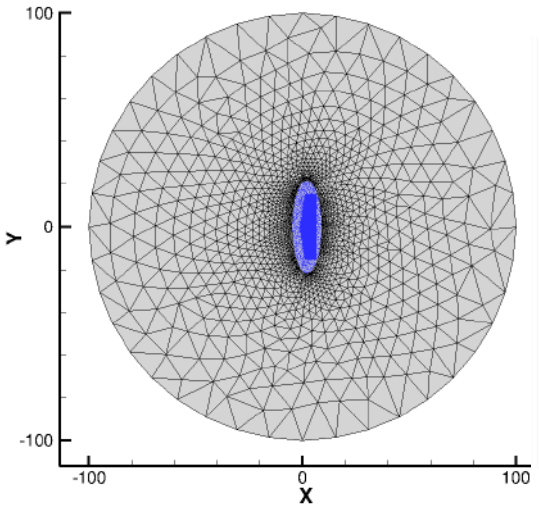


(c) Full computational domain.

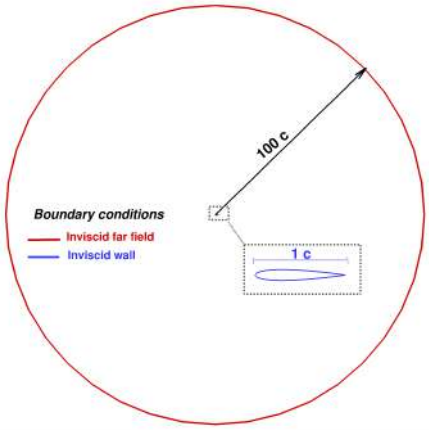


(d) Prescribed boundary conditions

**Fig. 7 Computational domain and baseline triangular mesh used for the AGARD03 test-case.**

on the baseline mesh with the SU2 calculation on the two feature-adapted meshes. The only minor difference between the un-adapted and feature-adapted calculations has to do with the location of the nearly normal shock, see Fig. 9b, which is likely due to the very different mesh spacing, resp. h/c = 0.03 vs. h/c = 0.009, between the two types of grids in that region, see Fig. 10c.

The comparison between the shock-capturing calculations and the hybrid shock-fitting one confirms the reliability of the latter, which will be used in Sect. IV to draw the key findings of this study. The fully-fitted simulation to be described in Sect. V will further corroborate the conclusions put forth in Sect. IV.

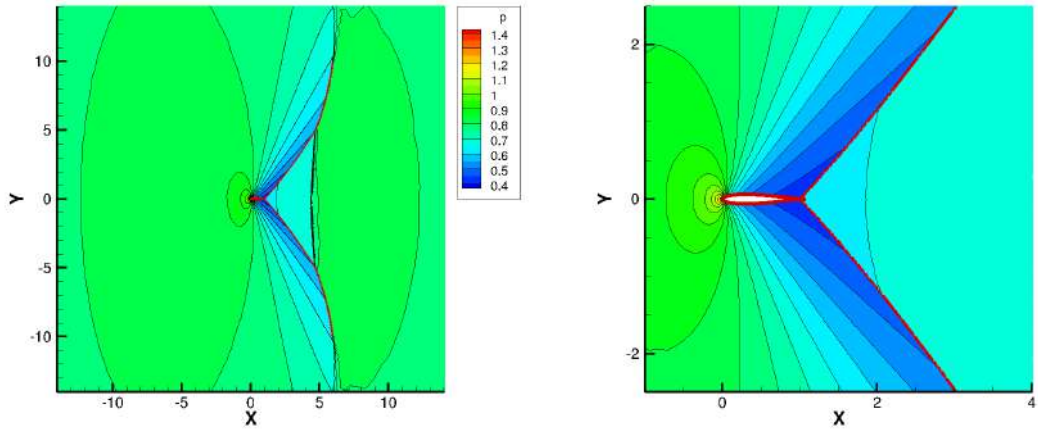


(a) Hybrid shock-fitting: overall view.

(b) Hybrid shock-fitting: close-up around the airfoil.

**Fig. 8 AGARD03 test-case: pressure field computed using the hybrid shock-fitting approach and the baseline mesh.**

| Grid level | # nodes | # elements | Finest spacing (h/c) |
|---|---|---|---|
| 0 | 139570 | 278753 | 0.030 |
| 1 | 220107 | 439917 | 0.009 |
| 2 | 291532 | 582767 | 0.009 |

**Table 1 SU2 computations: characteristics of the un-adapted (level 0 or baseline) and feature-adapted grids**

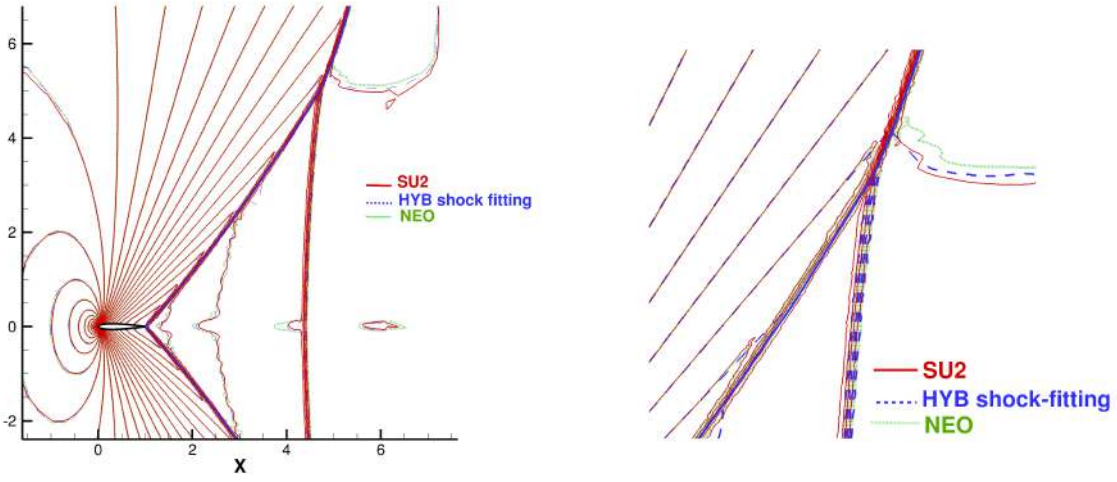


(a) Hybrid shock-fitting vs. shock-capturing solutions: close-up around the airfoil.

(b) Hybrid shock-fitting vs. shock-capturing solutions: close-up around the TP.

**Fig. 9 AGARD03 test-case: comparison among the Mach number iso-contour lines computed using different CFD codes on the baseline mesh.**

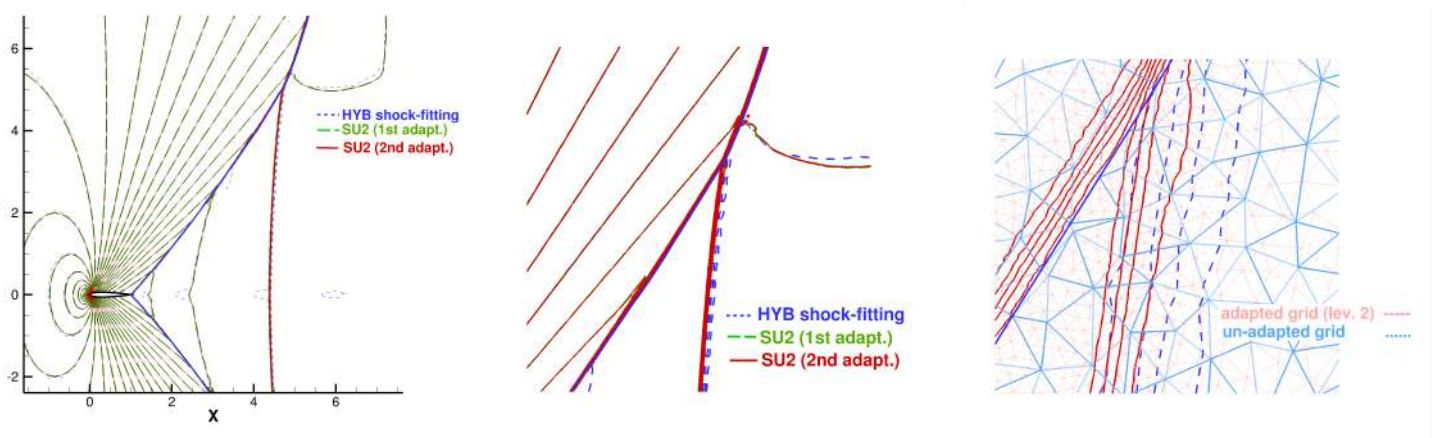


(a) Close-up around the airfoil. (b) Close-up around the TP. (c) Adapted vs un-adapted grid around the TP.

**Fig. 10 AGARD03 test-case: Mach iso-contour lines computed using hybrid shock-fitting on the baseline grid and fully-captured SU2 calculations on the feature-adapted level 1 and 2 grids.**

## IV. Analysis of the hybrid shock-fitting solutions

Making use of the taxonomy discussed in Sect. II.D and using data of the hybrid shock-fitting calculation described in Sect. III we want to establish whether the TP arising in the fishtail shock-interaction is compatible with either von Neumann's 3ST or Guderley's 4WT. This can be ascertained by looking at the position of the $(M_1, \sigma_{12})$ pair at the TP inside the plane of Fig. 4. We have extracted the $(M_1, \sigma_{12})$ values along the I-shock (the oblique shock), starting near the TE of the airfoil and up to a location (labeled 151 in Fig. 11a) close to where the captured R-shock (the nearly normal shock) joins the fitted I-shock (the oblique shock). Figure 11a displays the numbering of the grid-points along the I-shock on top of the computed pressure field. The corresponding $(M_1, \sigma_{12})$ values are plot in Fig. 11b were are also shown: the first Henderson line, which marks the boundary between the 3ST (to its right) and the 4WT (to its left) and the boundary separating the Vasil'ev ($M_4 < 1$) and Guderley ($M_4 > 1$) solutions to the 4WT.

Inspection of Fig. 11b clearly reveals that the 3ST cannot be applied to describe the three-shocks confluence occurring at the TP of the fishtail. Indeed, those points along the I-shock which are closer to the TP (e.g. grid-point 151 in Fig. 11a), are those further away from the first Henderson line, the leftmost boundary of the $(M_1, \sigma_{12})$ plane where (physically plausible) solutions to the 3ST exists. Therefore, Figure 11b suggests that the three shock confluence that characterizes the fishtail structure should be modeled using the 4WT instead. We have thus computed the solution to the 4WT using the $(M_1, \sigma_{12})$ values at point 151 of Fig. 11a; the results are reported in Appendix VI, as well as in Fig. 6b, where the 4WT solution in shown in the $(p, \theta)$ plane.

The same analysis, described so far for the AGARD03 test-case, has been repeated for decreasing values of the free-stream Mach number down to $M_\infty = 0.91$. The corresponding Mach isolines computed using the hybrid shock-fitting approach are shown in the five frames of Fig. 12: it can be seen that the nearly normal shock moves

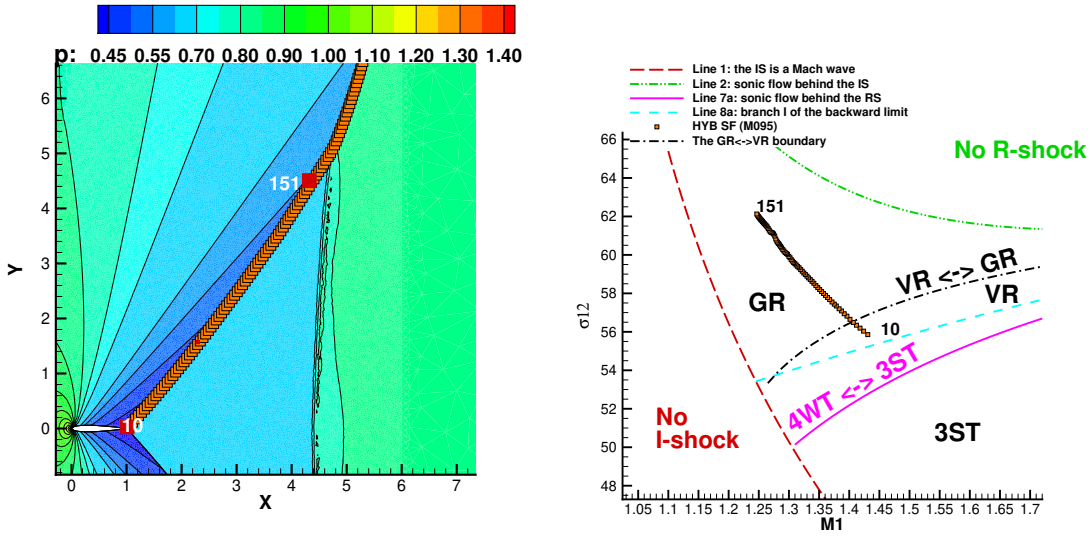


(a) Pressure field and numbering of the grid-points along the I-shock.

(b) Location within the $(M_1, \sigma_{12})$ plane of the values computed along the I-shock.

**Fig. 11 AGARD03 test-case: position in the $(x, y)$ and $(M_1, \sigma_{12})$ planes of the points located along the fitted I-shock.**

upstream towards the TE of the airfoil when the free-stream Mach number decreases.

One of the reviewers pointed us to the transition between the different shock-patterns observed in transonic flows at nearly sonic speed, which is well described in [53]:

> as $M_\infty$ approaches one from below, the shock moves toward the trailing edge of the airfoil [...] The shock actually hits the tail for some $M_\infty < 1$, there after a second, fishtail shock forms.

For the NACA0012 at zero angle-of-attack, we have numerically verified that the shock hits the TE between $M_\infty = 0.89$, when two separate shocks reach the upper and lower sides of the airfoil ahead of the TE, and $M_\infty = 0.90$, when the fishtail has already appeared. The capability of fitting (rather than capturing) the shock waves might prove useful to analyze the "second" that marks the transition between the two aforementioned shock-patterns.

Similarly to Fig. 11b, Fig. 12f shows the position within the $(M_1, \sigma_{12})$ plane of only one grid-point, picked-up along the I-shock and close to the TP, for each of the five different free-stream Mach numbers examined. Figure 12f reveals that, by decreasing the free-stream Mach number, the point on the I-shock close to the TP approaches line 8a, but without reaching it, thus always remaining inside the von Neumann region. As a result, the 3ST cannot describe the TP of the fishtail regardless of the free-stream Mach number, and the 4WT should be used instead. Furthermore, Figure 12f shows that four out of the five points, corresponding to different values of the free-stream Mach number, fall inside the GR, and only the one corresponding to $M_\infty = 0.91$ inside the VR region.

As already mentioned in Sect. II, in the hybrid simulation the TP is not a geometrical point, but rather a region of finite thickness, spanning two to three triangular cells. This implies that the location of the TP in the hybrid simulation

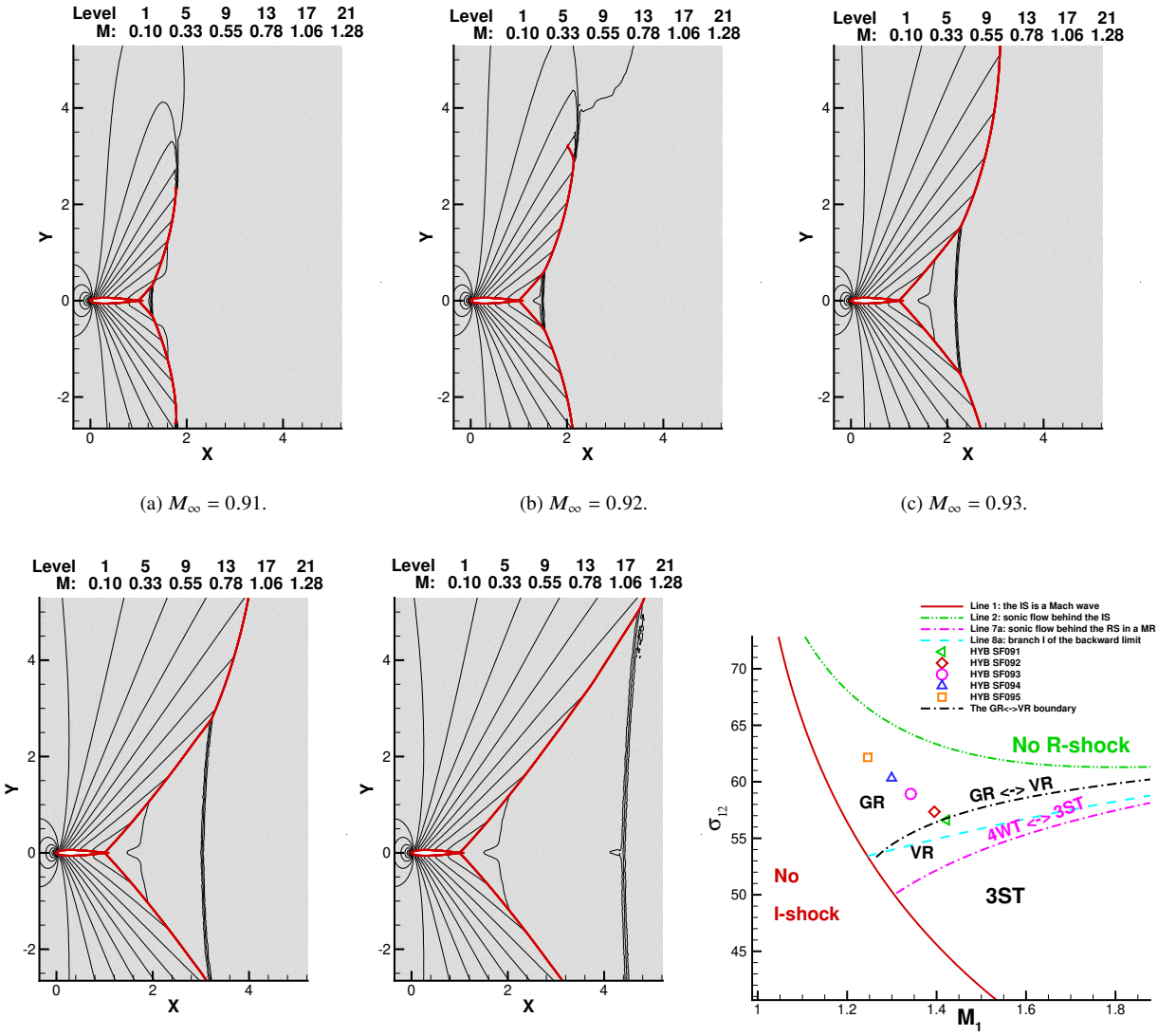


(a) $M_\infty = 0.91$. (b) $M_\infty = 0.92$. (c) $M_\infty = 0.93$.

(d) $M_\infty = 0.94$. (e) $M_\infty = 0.95$. (f) $(M_1, \sigma_{12})$ plane.

**Fig. 12 Hybrid shock-fitting solutions for different free-stream Mach numbers and position in the $(M_1, \sigma_{12})$ plane of the point along the oblique shock closest to the TP; fitted shocks are marked using red solid lines, Mach iso-contour lines are shown in frames (a) to (d)**

is affected by a geometrical uncertainty which has an impact on the corresponding $(M_1, \sigma_{12})$ values. The fully-fitted simulation to be presented in Sect. V aims at showing that the aforementioned uncertainty does not qualitatively affect the conclusions drawn here.

## V. Analysis of the fully-fitted solution

To verify the findings reported in Sect. IV, the shock interaction model based on the 4WT was coded in the *UnDiFi-2D* software, so as to allow a fully-fitted simulation of the AGARD-03 test-case. The 4WT model is very similar to the one already available in the *UnDiFi-2D* code to deal with the branching point (quadrupole point) arising from the interaction between two shocks of the same family, whose algorithmic details have been reported in [40]. The only difference between the two interaction models lies in the fact that the slope of the R-shock of Fig. 3b must be the one corresponding to sonic downstream flow, Eq. 2d. Moreover, in order to retain the similarity between the two interaction models, the expansion fan in Fig. 3b is computed using the R-H relations, rather than the Prandtl-Mayer ones. This is however an acceptable approximation in our case, because the expansion fan arising in GR/VR is very weak, see Tab. 2.

The Mach flow field computed using the fully-fitted simulation is displayed in Fig. 13a: the fitted discontinuities are marked using black solid lines, whereas the sonic line is drawn using a white line. The zoom centered around the branching point confirms that the fully-fitted solution is able to reproduce the key features of the GR, including the supersonic patches on both sides of the SS, despite the use of a rather coarse mesh. The comparison between the fully-fitted solution on the baseline grid and the fully-captured `SU2` simulation on the level 2 grid is reported in Fig. 9: it shows only a tiny difference in the location of the nearly normal shock, see Fig. 14b. However, closer inspection of the Mach iso-contour lines reveals that, despite the use of a mesh which is approximately three times finer than the baseline one, see Fig. 10c, the fully-captured solution misses the supersonic patches on both sides of the SS.

Even more important for the purpose of the present study, the availability of the fully-fitted solution supplies the $(M_1, \sigma_{12})$ values precisely at the TP. When these are compared against the corresponding values extracted from the hybrid simulation, as we do in Fig. 13b, good agreement is found, which confirms the conclusion drawn in Sect. IV.

## VI. Conclusions

The fishtail shock-interaction pattern that develops around a NACA0012 profile flying at transonic speed and zero angle of attack features two symmetric branching points where different discontinuities meet. Combining numerical simulations and classical shock-polar analysis, we show that von Neumann's three-shock theory cannot be used to model the local flow-field at the branching points of the fishtail. Instead, Guderley's four-wave theory, which postulates an additional expansion fan centered at the branching point, appears to be consistent with the data obtained from the numerical simulations. Even though the shock-capturing and the hybrid shock-capturing/shock-fitting calculations return almost identical steady-state solutions of the fishtail pattern, none of the two reveals the expansion fan. Only the

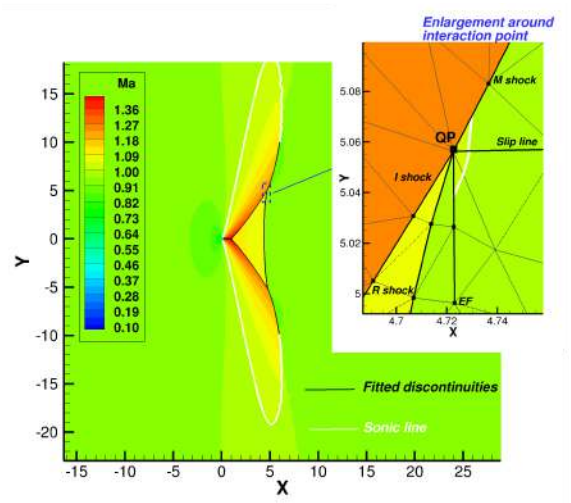


(a) Fully-fitted solution: Mach number field and detail around the TP

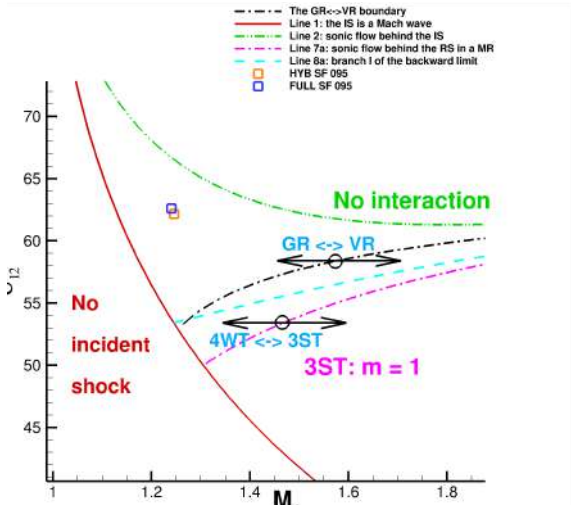


(b) Hybrid vs. fully-fitted $(M_1, \sigma_{12})$ pairs at the TP

**Fig. 13 AGARD03 test-case: fully-fitted solution and TP values in the $(M_1, \sigma_{12})$ plane**

fully-fitted calculation, which models the branching point using the four-waves theory, reveals the presence of a weak expansion fan in the interaction region.

## Appendix: Boundaries in the $(M_1, \sigma_{12})$ plane.

We list here the equations required to draw those lines in the $(M_1, \sigma_{12})$ plane, see Fig. 4, which we referred to throughout the paper. This is only a small subset of the numerous lines that bound regions of the $(M_1, \sigma_{12})$ where different shock-interaction patterns are observed. The interested reader is referred to [2, 8, 54, 55] for a more extensive discussion. See also [18] and [13] where these same boundaries are drawn in the $(M_1, \theta_{12})$ and $(M_1, \xi_{21})$ planes. The labeling of the lines used here follows [8].

- Line 1: the incident shock (IS) is a Mach wave

  On line 1 the I-shock has zero strength, i.e. it is a Mach wave; therefore, the I-shock angle is the Mach angle:

$$\sigma_{12} = \sin^{-1}\left(\frac{1}{M_1}\right) \tag{1}$$

- Line 2: Sonic flow behind I-shock

  Shock-shock interaction is possible only as long as the flow behind the I-shock is supersonic, i.e. $M_2 > 1$. The I-shock angle corresponding to the limit condition of sonic flow behind the I-shock can be computed from [56, Eq. (167)] using the given value of $M_1$.

- Line 7a (the first Henderson line): sonic flow behind the R-shock in the 3ST.

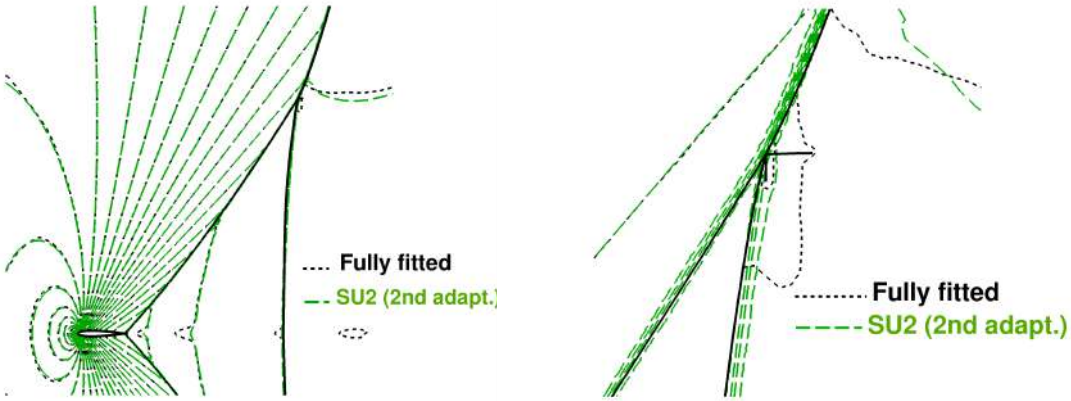


(a) Fully-fitted vs. shock-capturing solutions (SU2): close-up around the airfoil.

(b) Fully-fitted vs. shock-capturing (SU2): close-up around the TP.

**Fig. 14 AGARD03 test-case: comparison between the Mach iso-contour lines computed using SU2 on the level 2 grid and the fully-fitted calculation on the baseline mesh.**

The flow behind the R-shock in the 3ST is sonic along two distinct lines (the first and second Henderson line) of the $(M_1, \sigma_{12})$ plane, but only the first Henderson line is of interest when the I-shock is weak. Points on line 7a are solutions to the following 4×4 non-linear system of algebraic equations:

$$\sin^2 \sigma_{14} = \frac{(\gamma-1)(\gamma+1)+4\left[\gamma M_1^2 \sin^2\sigma_{12}-\delta\right]\left[\gamma M_2^2 \sin^2\sigma_{23}-\delta\right]}{2\gamma(\gamma+1)M_1^2} \tag{2a}$$

$$\theta(M_1, \sigma_{14}) = \theta(M_1, \sigma_{12}) + \theta(M_2, \sigma_{23}) \tag{2b}$$

$$M_2^2 = \frac{\left(1+\delta M_1^2 \sin^2\sigma_{12}\right)^2 + \left(\frac{1}{2}(\gamma+1) M_1^2 \sin\sigma_{12}\cos\sigma_{12}\right)^2}{\left(1+\delta M_1^2 \sin^2\sigma_{12}\right)\left(\gamma M_1^2 \sin^2\sigma_{12}-\delta\right)} \tag{2c}$$

$$\sin^2 \sigma_{23} = \frac{(\gamma-3)+(\gamma+1)M_2^2+\sqrt{(\gamma+1)\left[(\gamma+9)+2(\gamma-)M_2^2+(\gamma+1)M_2^4\right]}}{4\gamma M_2^2} \tag{2d}$$

Equations (2a) and (2b) respectively translate the conditions of equal pressure and flow direction across the SS. Equation (2c) is [56, Eq. (132)] and gives the Mach number behind the I-shock as a function of $M_1$ and the I-shock angle. Equation (2d) is [56, Eq. (167)] and gives the R-shock angle corresponding to sonic flow behind the R-shock, i.e. $M_3 = 1$. The flow deflection $\theta$ in Eqs. (2b) is computed from [56, Eq. (138)]. The four unknowns in the system (2) are: $M_2, \sigma_{12}, \sigma_{23}, \sigma_{14}$, whereas $M_1$ is given. The $(M_1, \sigma_{12})$ coordinates of the point where the first Henderson line joins line 1 can be computed as described in [54].

- Line 8a: branch I of the backward limit in the 3ST.

  Physically, the backward limit corresponds to a three-shocks-system in which the R-shock is a Mach wave, which implies that the I-shock and M-shock form a unique shock. A simple closed-form expression that allows to draw

the backward limit is attributed by Henderson [18, Eqs. (15-16)] to Wecken [57] and it is repeated here:

$$M_1^2 = \frac{1+\xi_i/\mu^2}{\xi_i\, U_\pm} - \frac{2}{\gamma-1} \tag{3a}$$

where:

$$U_\pm \;=\; 1 + \frac{2\,\mu^2\,\xi_i}{1+\xi_i \pm \sqrt{\left(1+\mu^2\,\xi_i\right)\left(1+\xi_i/\mu^2\right)}} \tag{3b}$$

In Eqs. (3) $\xi_i = \xi_{12}^{-1}$ i.e. the inverse pressure ratio across the I-shock. There are two branches of the backward limit, but only branch I, which corresponds to the plus sign in Eq. (3b), is of interest in the range of Mach number considered here. Line 8a is drawn by taking values of $\xi_i$ ranging between 1 (which corresponds to the point where line 8a joins line 1) and a pre-set value smaller than 1. $M_1$ is then computed from Eq. (3a) and the I-shock angle, $\sigma_{12}$, follows from [56, Eq. (128)].

## Appendix: four waves theory (4WT).

The set of non-linear algebraic equations governing the 4WT can be found in [21]. It is however worth recalling it here. Given the free-stream Mach number, $M_1$ and I-shock angle, $\sigma_{12}$, which are the same two input parameters also used in the 3ST, the following quantities behind the I-shock can be easily computed: the flow deflection, $\theta_{12}$, and pressure ratio, $\xi_{21}$, across the I-shock and the Mach number, $M_2$, in the region bounded by the I- and R-shocks. Since the flow behind the R-shock is sonic in the 4WT, i.e. $M_3 = 1$, the R-shock angle, $\sigma_{23}$, can be computed from [56, Eq. (167)] using the known value of $M_2$. The pressure ratio across the R-shock, $\xi_{32}$, follows from [56, Eq. (128)] using the known values of $M_2$ and $\sigma_{23}$. The flow across the EF is isentropic, therefore:

$$\frac{p_5}{p_3} = \left[\frac{1+\delta\,M_5^2}{(\gamma+1)/2}\right]^{-\frac{\gamma}{\gamma-1}}$$

The two conditions that hold across the SS, i.e. equal flow direction and equal pressure, can be translated into the following two by two non-linear system of algebraic equations:

$$\theta\left(M_1,\sigma_{14}\right) - \nu\left(M_5\right) \;=\; \theta_{12}+\theta_{23} \tag{4a}$$

$$\xi\left(M_1,\sigma_{14}\right)\left[\frac{1+\delta\,M_5^2}{(\gamma+1)/2}\right]^{\frac{\gamma}{\gamma-1}} \;=\; \xi_{32}\,\xi_{21} \tag{4b}$$

where terms on the r.h.s. are known and the only two unknowns appear on the l.h.s. These are: the (supersonic) Mach number, $M_5$, in the region bounded by the tail of the EF and the SS and the M-shock angle, $\sigma_{14}$. In Eqs. (4) $\theta$ and $\xi$ are

the flow deflection and pressure ratio through an oblique shock, which can be computed using [56, Eq. (138)] and [56, Eq. (128)], respectively; $\nu(M)$ is the Prandtl-Meyer function [56, Eq. (171c)].

Two sample applications of the 4WT are listed in Tab. 2. The left column of Table 2, which refers to Fig. 6a, shows both the 3ST and 4WT solutions for the point marked with a square in Fig. 4. According to [17], it is the 4WT solution which should be chosen inside the first Henderson region. The right column of Tab. 2, which refers to Fig. 6b, lists the 4WT solution at point 151 of Fig. 11a, which is the point along the fitted I-shock that is closest to the TP region of the fishtail in the AGARD03 test-case.

**Table 2 Features of the VR and GR shown in Fig. 6; input data are $M_1$ and $\sigma_{12}$.**

| Vasi'lev reflection of Fig. 6a | | |
|---|---|---|
| | 3ST | 4WT |
| $\xi_{53}$ | - | 0.99532 |
| $M_5$ | - | 1.00401 |
| $\theta_{35}$ | - | 0.01142 |
| $\xi_{41}$ | 1.59762 | 1.81053 |
| $\sigma_{14}$ | 57.335 | 63.02324 |
| $M_4$ | 1.1052 | 0.99229 |
| $\theta_{14}$ | 9.10869 | 10.73184 |
| $\xi_{21}$ | 1.5 | 1.5 |
| $\sigma_{12}$ | 54.9069 | 54.90695 |
| $M_2$ | 1.1581 | 1.15810 |
| $\theta_{12}$ | 8.03923 | 8.03923 |
| $\xi_{32}$ | 1.06508 | 1.21269 |
| $\sigma_{23}$ | 62.5286 | 69.86787 |
| $M_3$ | 1.10812 | 1.00000 |
| $\theta_{23}$ | 1.06946 | 0.04680 |
| $M_1$ | 1.46077 | 1.46077 |

| Guderley reflection of Fig. 6b | |
|---|---|
| | 4WT |
| $\xi_{53}$ | 0.99006 |
| $M_5$ | 1.00854 |
| $\theta_{35}$ | .03531 |
| $\xi_{41}$ | 1.34599 |
| $\sigma_{14}$ | 66.04472 |
| $M_4$ | 1.00727 |
| $\theta_{14}$ | 4.80818 |
| $\xi_{21}$ | 1.24948 |
| $\sigma_{12}$ | 62.15677 |
| $M_2$ | 1.07076 |
| $\theta_{12}$ | 3.91812 |
| $\xi_{32}$ | 1.08805 |
| $\sigma_{23}$ | 75.58431 |
| $M_3$ | 1.00000 |
| $\theta_{23}$ | 0.01492 |
| $M_1$ | 1.24600 |

**The boundary between the VR and GR in the 4WT**

The boundary between the Vasilev ($M_4 < 1$) and Guderley ($M_4 > 1$) reflection corresponds to the condition of sonic flow behind the M-shock in the 4WT. i.e. $M_4 = 1$. Using $M_1$ as the free parameter, the shock-angle, $\sigma_{14}$, and flow deflection across the M-shock, $\theta_{14}$, must be those corresponding to sonic flow behind an oblique shock and can be readily computed from [56, Eq. (167)] and [56, Eq. (138)].

The system of non-linear algebraic equations to be solved is the following:

$$\theta_{14} = \theta_{12}\left(M_1, \sigma_{12}\right) + \theta_{23}\left(M_2, \sigma_{23}\right) + \nu\left(M_5\right) \tag{5a}$$

$$\xi_{41} = \xi_{21}\left(M_1, \sigma_{12}\right)\xi_{32}\left(M_2, \sigma_{23}\right)\left[\frac{1+\delta\, M_5^2}{(\gamma+1)/2}\right]^{-\frac{\gamma}{\gamma-1}} \tag{5b}$$

$$\sin^2\sigma_{23} = \frac{(\gamma-3)+(\gamma+1)\,M_2^2+\sqrt{(\gamma+1)\left[(\gamma+9)+2\,(\gamma-3)\;M_2^2+(\gamma+1)\,M_2^4\right]}}{4\,\gamma\,M_2^2} \tag{5c}$$

$$M_2^2 = \frac{\left(1+\delta\,M_1^2\sin^2\sigma_{12}\right)^2+\left(\frac{1}{2}\,(\gamma+1)\;M_1^2\sin\sigma_{12}\cos\sigma_{12}\right)^2}{\left(1+\delta\,M_1^2\sin^2\sigma_{12}\right)\left(\gamma\,M_1^2\sin^2\sigma_{12}-\delta\right)} \tag{5d}$$

Equations (5a) and (5b) translate the conditions of parallel streams and equal pressure across the SS; the various functions involved have already been defined by reference to Eq. (4). Equations (5c) and (5d) have also been already introduced by reference to Eq. (2).

The l.h.s. of Eqs. (5a) and (5b) is known for the reasons stated above, so that the four unknowns in (5) are: $M_2, M_5, \sigma_{12}, \sigma_{23}$.

## References


[1] Shell Film Unit, "High Speed Flight : Part 2 -Transonic Flight," YouTube, 1959. URL `https://www.youtube.com/watch?v=QOzdY3m-1a8`, uploaded by National Aerospace Library.

[2] Hornung, H., "Regular and Mach reflection of shock waves," Annual Review of Fluid Mechanics, Vol. 18, No. 1, 1986, pp. 33–58. https://doi.org/10.1146/annurev.fl.18.010186.000341.

[3] Krehl, P., and van der Geest, M., "The discovery of the Mach reflection effect and its demonstration in an auditorium," Shock Waves, Vol. 1, No. 1, 1991, pp. 3–15. https://doi.org/10.1007/BF01414863.

[4] Courant, R., and Friedrichs, K. O., Supersonic Flow and Shock Waves, fourth edition 1963 ed., Pure and Applied mathematics, Vol. I, Interscience Publishers, New York, 1948.

[5] Von Neumann, J., "Oblique reflection of shocks," Bureau of Ordinance, Explosives Research Report, 1943.

[6] Von Neumann, J., "Theory of shock waves," Tech. rep., Institute for Advanced Study Princeton, NJ, 1943. URL https://apps.dtic.mil/sti/pdfs/ADB805024.pdf.

[7] von Neumann, J., The Collected Works of John von Neumann: Volume VI: Theory of Games, Astrophysics, Hydrodynamics and Meteorology, Pergamon Press, 1963.

[8] Chapman, C. J., High speed flow, Cambridge University Press, 2000.

[9] Pain, H. J., and Rogers, E. W. E., "Shock waves in gases," Reports on Progress in Physics, Vol. 25, No. 1, 1962, pp. 287–336. https://doi.org/10.1088/0034-4885/25/1/308.

[10] Bargmann, V., and Montgomery, D., Report 5011, O.S.R.D., 1945.

[11] Guderley, K. G., "Considerations of the structure of mixed subsonic-supersonic flow patterns," Air material command tech. report, F-TR-2168-ND, ATI No. 22780, U.S. Wright-Patterson Air Force Base, GS-AAF-Wright Field 39, Dayton, Ohio., oct 1947. URL https://books.google.it/books?id=p7uMswEACAAJ&printsec=frontcover&hl=it&source=gbs_ge_summary_r&cad=0#v=onepage&q&f=false.

[12] Guderley, K. G., Theory of Transonic Flow, Pergamon Press, 1962.

[13] Kalghatgi, G. T., and Hunt, B. L., "The Three-Shock Confluence Problem for Normally Impinging, Overexpanded Jets," Aeronautical Quarterly, Vol. 26, No. 2, 1975, p. 117–132. https://doi.org/10.1017/S0001925900007265.

[14] South, J. C. J., Thomas, J. L., and Van Rosendale, J. (eds.), ICASE/LaRC Workshop on Adaptive Grid Methods, 1995. URL https://ntrs.nasa.gov/citations/19960011635.

[15] Richter, R., and Leyland, P., "Auto-adaptive finite element meshes," NASA Langley Research Center, ICASE (LaRC Workshop on Adaptive Grid Methods, 1995, pp. 219–232. URL https://ntrs.nasa.gov/citations/19960011650.

[16] Ait-Ali-Yahia, D., Baruzzi, G., Habashi, W. G., Fortin, M., Dompierre, J., and Vallet, M.-G., "Anisotropic mesh adaptation: towards user-independent, mesh-independent and solver-independent CFD. Part II. Structured grids," International Journal for Numerical Methods in Fluids, Vol. 39, No. 8, 2002, pp. 657–673. https://doi.org/10.1002/fld.356.

[17] Ben-Dor, G., Shock wave reflection phenomena, Springer Verlag, 2007.

[18] Henderson, L. F., "On the confluence of three shock waves in a perfect gas." Aeronautical Quarterly, Vol. 15(2), 1964, pp. 181–197. https://doi.org/10.1017/S0001925900003115.

[19] Hunter, J. K., and Brio, M., "Weak shock reflection," Journal of Fluid Mechanics, Vol. 410, 2000, p. 235–261. https://doi.org/10.1017/S0022112099008010.

[20] Vasil'ev, E. I., "The nature of the triple point singularity in the case of stationary reflection of weak shock waves," Fluid Dynamics, Vol. 51, No. 6, 2016, pp. 804–813. https://doi.org/10.1134/S0015462816060119.

[21] Vasilev, E. I., Elperin, T., and Ben-Dor, G., "Analytical reconsideration of the von Neumann paradox in the reflection of a shock wave over a wedge," Physics of Fluids, Vol. 20, No. 4, 2008, p. 046101. https://doi.org/10.1063/1.2896286.

[22] Tesdall, A. M., Sanders, R., and Popivanov, N., "Further Results on Guderley Mach Reflection and the Triple Point Paradox," Journal of Scientific Computing, Vol. 64, No. 3, 2015, pp. 721–744. https://doi.org/10.1007/s10915-015-0028-1.

[23] Kobayashi, S., Adachi, T., and Suzuki, T., "Examination of the von Neumann paradox for a weak shock wave," Fluid Dynamics Research, Vol. 17, No. 1, 1995, pp. 13–25. https://doi.org/https://doi.org/10.1016/0169-5983(95)00020-E.

[24] Birkhoff, G., "Hydrodynamics: A study in logic, fact, and similitude," Bull. Amer. Math. Soc, Vol. 57, 1951, pp. 97–499.

[25] Skews, B. W., and Ashworth, J. T., "The physical nature of weak shock wave reflection," Journal of Fluid Mechanics, Vol. 542, 2005, p. 105–114. https://doi.org/10.1017/S0022112005006543.

[26] Skews, B. W., Li, G., and Paton, R., "Experiments on Guderley Mach reflection," Shock Waves, Vol. 19, No. 2, 2009, pp. 95–102. https://doi.org/10.1007/s00193-009-0193-y.

[27] Cachucho, A., and Skews, B. W., "Guderley reflection for higher Mach numbers in a standard shock tube," Shock Waves, Vol. 22, No. 2, 2012, pp. 141–149. https://doi.org/10.1007/s00193-011-0349-4.

[28] Vasil'ev, E. I., "High resolution simulation for the Mach Reflection of Weak Shock Waves," Proc. of the ECCOMAS 4th Computational Fluid Dynamics Conference, Vol. 1, edited by K. D. Papailiou, John Wiley & Sons, Ltd., 1998, pp. 520–527. Athens, Greece (7-11) Sept. 1998.

[29] Vasil'ev, E. I., "Four-wave scheme of weak Mach shock wave interaction under von Neumann paradox conditions," Fluid Dynamics, Vol. 34, No. 3, 1999, pp. 421—427.

[30] Zakharian, A. R., Brio, M., Hunter, J. K., and Webb, G. M., "The von Neumann paradox in weak shock reflection," Journal of Fluid Mechanics, Vol. 422, 2000, p. 193–205. https://doi.org/10.1017/S0022112000001609.

[31] Tesdall, A. M., and Hunter, J. K., "Self-Similar Solutions for Weak Shock Reflection," SIAM Journal on Applied Mathematics, Vol. 63, No. 1, 2002, pp. 42–61. https://doi.org/10.1137/S0036139901383826.

[32] Tesdall, A. M., Sanders, R., and Keyfitz, B. L., "The Triple Point Paradox for the Nonlinear Wave System," SIAM Journal on Applied Mathematics, Vol. 67, No. 2, 2007, pp. 321–336. https://doi.org/10.1137/060660758.

[33] Defina, A., Susin, F. M., and Viero, D. P., "Numerical study of the Guderley and Vasilev reflections in steady two-dimensional shallow water flow," Physics of Fluids, Vol. 20, No. 9, 2008, p. 097102. https://doi.org/10.1063/1.2972936.

[34] Defina, A., Viero, D. P., and Susin, F. M., "Numerical simulation of the Vasilev reflection," Shock Waves, Vol. 18, No. 3, 2008, pp. 235–242. https://doi.org/10.1007/s00193-008-0159-5.

[35] Ivanov, M., Shoev, G., Khotyanovsky, D., Bondar, Y., and Kudryavtsev, A., "Supersonic Patches in Steady Irregular Reflection of Weak Shock Waves," 28th International Symposium on Shock Waves, 2012, pp. 543–548. https://doi.org/10.1007/978-3-642-25685-1_82.

[36] Campoli, L., Assonitis, A., Ciallella, M., Paciorri, R., Bonfiglioli, A., and Ricchiuto, M., "UnDiFi-2D: an Unstructured Discontinuity Fitting code for 2D grids," Computer Physics Communications, Vol. 271, 2022, p. 108202. https://doi.org/10.1016/j.cpc.2021.108202, URL https://github.com/UnDiFi/UnDiFi-2D.

[37] Paciorri, R., and Bonfiglioli, A., "A shock-fitting technique for 2D unstructured grids," Computers & Fluids, Vol. 38, No. 3, 2009, pp. 715–726. https://doi.org/10.1016/j.compfluid.2008.07.007.

[38] Bonfiglioli, A., Paciorri, R., and Campoli, L., "Unsteady shock-fitting for unstructured grids," International Journal for Numerical Methods in Fluids, Vol. 81, No. 4, 2016, pp. 245–261. https://doi.org/10.1002/fld.4183.

[39] Ivanov, M. S., Bonfiglioli, A., Paciorri, R., and Sabetta, F., "Computation of weak steady shock reflections by means of an unstructured shock-fitting solver," Shock Waves, Vol. 20, No. 4, 2010, pp. 271–284. https://doi.org/10.1007/s00193-010-0266-y.

[40] Paciorri, R., and Bonfiglioli, A., "Shock interaction computations on unstructured, two-dimensional grids using a shock-fitting technique," Journal of Computational Physics, Vol. 230, No. 8, 2011, pp. 3155 – 3177. https://doi.org/10.1016/j.jcp.2011.01.018.

[41] Bonfiglioli, A., "Fluctuation splitting schemes for the compressible and incompressible Euler and Navier-Stokes equations," International Journal of Computational Fluid Dynamics, Vol. 14, No. 1, 2000, pp. 21–39. https://doi.org/10.1080/10618560008940713.

[42] Bonfiglioli, A., and Paciorri, R., "A mass-matrix formulation of unsteady fluctuation splitting schemes consistent with Roe's parameter vector," International Journal of Computational Fluid Dynamics, Vol. 27, No. 4-5, 2013, pp. 210–227. https://doi.org/10.1080/10618562.2013.813491.

[43] Bonfiglioli, A., and Paciorri, R., "Convergence analysis of shock-capturing and shock-fitting solutions on unstructured grids," AIAA J., Vol. 52, No. 7, 2014, pp. 1404–1416. https://doi.org/10.2514/1.J052567.

[44] Donat, R., and Osher, S., "Propagation of error into regions of smoothness for non-linear approximations to hyperbolic equations," Computer Methods in Applied Mechanics and Engineering, Vol. 80, No. 1, 1990, pp. 59–64. https://doi.org/https://doi.org/10.1016/0045-7825(90)90014-D.

[45] Carpenter, M. H., and Casper, J. H., "Accuracy of Shock Capturing in Two Spatial Dimensions," AIAA Journal, Vol. 37, No. 9, 1999, pp. 1072–1079. https://doi.org/10.2514/2.835.

[46] Shewchuk, J. R., "Triangle: Engineering a 2D Quality Mesh Generator and Delaunay Triangulator," Applied Computational Geometry: Towards Geometric Engineering, Lecture Notes in Computer Science, Vol. 1148, edited by M. C. Lin and D. Manocha, Springer-Verlag, 1996, pp. 203–222. From the First ACM Workshop on Applied Computational Geometry.

[47] Muller, J.-D., Roe, P. L., and Deconinck, H., "A frontal approach for internal node generation in Delaunay triangulations," International Journal for Numerical Methods in Fluids, Vol. 17, No. 3, 1993, pp. 241–255. https://doi.org/10.1002/fld.1650170305.

[48] Ricchiuto, M., and Abgrall, R., "Explicit Runge-Kutta residual distribution schemes for time dependent problems: Second order case," Journal of Computational Physics, Vol. 229, No. 16, 2010, pp. 5653 – 5691. https://doi.org/10.1016/j.jcp.2010.04.002.

[49] Ricchiuto, M., "An explicit residual based approach for shallow water flows," Journal of Computational Physics, Vol. 280, 2015, pp. 306 – 344. https://doi.org/https://doi.org/10.1016/j.jcp.2014.09.027.

[50] Economon, T. D., Palacios, F., Copeland, S. R., Lukaczyk, T. W., and Alonso, J. J., "SU2: An Open-Source Suite for Multiphysics Simulation and Design," AIAA Journal, Vol. 54, No. 3, 2016, pp. 828–846. https://doi.org/10.2514/1.J053813, URL https://doi.org/10.2514/1.J053813.

[51] Dobrzynski, C., and Frey, P., "Anisotropic Delaunay mesh adaptation for unsteady simulations," Proceedings of the 17th international Meshing Roundtable, Springer, 2008, pp. 177–194. URL https://hal.science/hal-00353786.

[52] Dapogny, C., Dobrzynski, C., and Frey, P., "Three-dimensional adaptive domain remeshing, implicit domain meshing, and applications to free and moving boundary problems," Journal of computational physics, Vol. 262, 2014, pp. 358–378. https://doi.org/https://doi.org/10.1016/j.jcp.2014.01.005.

[53] Cook, L. P., and Zeigler, F. J., "The Stabilization Law for Transonic Flow," SIAM Journal on Applied Mathematics, Vol. 46, No. 1, 1986, pp. 27–48. https://doi.org/https://doi.org/10.1137/0146004, URL http://www.jstor.org/stable/2101485.

[54] Mouton, C. A., "Transition between Regular Reflection and Mach Reflection in the Dual-Solution Domain," Ph.D. thesis, California Institute of Technology, Pasadena, California, USA, 2007. URL https://thesis.library.caltech.edu/36/1/ThesisRootFinal.pdf.

[55] Uskov, V. N., and Chernyshov, M. V., "Special and extreme triple shock-wave configurations," Journal of Applied Mechanics and Technical Physics, Vol. 47, 2006, pp. 492–504. https://doi.org/10.1007/s10808-006-0081-5.

[56] Ames Research Staff, "Equations, tables, and charts for compressible flow," Tech. rep., NASA Ames Research Centre, 1953. URL http://naca.larc.nasa.gov/reports/1953/naca-report-1135/, NACA Report 1135.

[57] Wecken, F., "Grenzlagen gegabelter Verdichtungsstöße," ZAMM-Journal of Applied Mathematics and Mechanics/Zeitschrift fur Angewandte Mathematik und Mechanik, Vol. 29, 1949, pp. 147–155.